



HAL
open science

Impact of a fragile precursor on the sintering of tin monoxide

Subhransu Subhasis Bhoi, Mathieu Duttine, U-Chan Chung, Michaël Josse, Matthew R. Suchomel

► **To cite this version:**

Subhransu Subhasis Bhoi, Mathieu Duttine, U-Chan Chung, Michaël Josse, Matthew R. Suchomel. Impact of a fragile precursor on the sintering of tin monoxide. Journal of the European Ceramic Society, In press. hal-03364257v1

HAL Id: hal-03364257

<https://hal.science/hal-03364257v1>

Submitted on 4 Oct 2021 (v1), last revised 26 Nov 2021 (v2)

HAL is a multi-disciplinary open access archive for the deposit and dissemination of scientific research documents, whether they are published or not. The documents may come from teaching and research institutions in France or abroad, or from public or private research centers.

L'archive ouverte pluridisciplinaire **HAL**, est destinée au dépôt et à la diffusion de documents scientifiques de niveau recherche, publiés ou non, émanant des établissements d'enseignement et de recherche français ou étrangers, des laboratoires publics ou privés.

Impact of a fragile precursor on the sintering of tin monoxide

Subhransu Subhasis Bhoi ^{a,b}, Mathieu Duttine ^{a,b}, U-Chan Chung ^{a,b}, Michaël Josse ^{a,b}, and Matthew R. Suchomel * ^{a, b}

^a Institut de Chimie de la Matière Condensée de Bordeaux (ICMCB), Pessac 33600, France

^b Université de Bordeaux, 351 cours de la Libération, 33405 Talence, France

* corresponding author

Keywords

Tin Monoxide; Ceramics; Spark Plasma Sintering; Metastable Materials; Low Temperature Densification

Abstract

The thermodynamic stability limits of Sn(II) under ambient conditions imposes constraints on the densification of divalent tin based oxides. In the case of tin monoxide (SnO), a low temperature (≤ 300 °C) electric field assisted processing route (Cool-SPS) affords densification up to 90% of theoretical density. This is demonstrated for both conventional SnO and fragile tin(II) oxyhydroxide [Sn₆O₄(OH)₄] precursor powders. The choice of starting precursor impacts both the optimized processing parameters and the resulting ceramic microstructure. Characterization of phase content and stability has been performed on both the precursor powders and resulting ceramics. Preliminary electrochemical property measurements are presented and their connection to observed microstructure and choice of initial precursor is discussed.

1. Introduction

From the perspective of both applied materials science and fundamental chemistry, divalent tin monoxide, also known as stannous oxide, is an intriguing compound with an unconventional history. Initial reports of synthetic SnO from the mid 1800's [1, 2] were later revisited in greater detail [3]. Similarly, the first descriptions of a two-dimensional layered tetragonal (*P4/nmm* space group) structure for α -SnO by Pauling *et al.* [4] were later refined with Rietveld analysis of neutron powder diffraction data [5] revealing how the sterically active lone pair Sn²⁺ cations form weak *van der Waals* bonds between sheets of covalently bonded SnO₄ pyramidal units. Unexpectedly, SnO was subsequently discovered as a naturally occurring mineral (with the assigned name Romarchite) forming via surface corrosion processes on Sn-rich metal alloys uncovered during archeological studies of sunken shipwreck sites, such as the pirate Blackbeard's ship *Queen Anne's Revenge* [6].

Recently this compound has received increased scrutiny for its prospects as a more environmentally friendly functional metal oxide in electronic and optoelectronic technological applications. Undoped, SnO is a *p*-type semiconducting metal oxide [7]. Multiple studies have examined its use in gas sensors, transparent conducting oxides, and thin film transistors [8, 9, 10]. Due to a relatively large interlayer spacing, SnO has also been considered as intercalation type electrode material for lithium and sodium-based energy storage applications [11, 12]. This two-dimensional structure type may also be associated with ferromagnetism, as recently predicted by first principles calculations for hole-doped SnO [13, 14]. In addition, theoretical and experimental studies have also investigated polycrystalline SnO as a potential thermoelectric material due to its relatively high Hall mobility [15].

Nevertheless, despite these intriguing properties and applications, processing of tin monoxide remains challenging. Metastable in its divalent oxidation state, blue-black Sn²⁺O undergoes disproportionation between 200 - 400 °C by a decomposition reaction to Sn⁴⁺O₂ and metallic Sn via an intermediary phase of Sn₃O₄. The precise decomposition temperatures vary with sample morphology, dwell time and atmospheric oxygen content [16, 17, 18]. Conventional high-temperature sintering routes therefore do not present feasible paths towards single phase dense SnO ceramics; instead, novel routes compatible with the low thermal stability limits of the compound need to be considered. Several low temperature sintering approaches have been developed in recent years [19], which includes Room Temperature Fabrication [20], Cold Sintering Processes [21], Hydrothermal

Sintering [22], and Cool-SPS [23]. These developing approaches can offer additional advantages in terms of energy efficiency, integrated co-sintering possibilities, and physical property tuning by control of nanocrystalline structures [24, 25]. For SnO, the effectiveness of a low temperature solvent assisted Cold Sintering Process (CSP) strategy was recently demonstrated [26]. In this CSP approach, relative densities of 80% - 90% are achieved in under 2 hours with uniaxial pressure at temperatures ≤ 265 °C. Vibratory ball milling of the initial commercial SnO precursor powders led to higher pellet densities after CSP processing due to decreased particle size and increased reactivity, although X-ray diffraction revealed the presence of SnO₂ above 200 °C.

In the current work presented here, we consider an alternative approach towards dense SnO ceramics by use of a Cool-SPS (SPS: Spark Plasma Sintering) method. SPS is a pressure assisted sintering technique using pulsed electric currents for heating. Initially targeted at rapid high temperature processing of metal and refractory materials, SPS has been increasingly examined as a versatile tool for the sintering and solid-state synthesis applicable to a broad class of materials [27]. Under lower processing temperatures (below 600 °C, within the pressure range 40 - 900 MPa) the Cool-SPS approach has recently been shown to be effective for the sintering of diverse thermodynamically unstable compounds; including molecular materials and oxides exploiting fragile precursors that convert into the desired phase upon processing [23, 28, 29]. In the current study reported here we extend this approach to processing of tin monoxide and consider the role of starting precursors in further enhancing reactivity during processing. Sn₆O₄(OH)₄ is explored as a fragile precursor and is compared with conventional tin(II) oxide powders. It is shown that with careful control of the processing conditions, highly dense SnO ceramics can be obtained from very different starting precursors, but with final microstructure and physical properties linked to the nature of the initial powders.

2. Experimental

2.1. Powder preparation

Synthesis of a tin(II) oxyhydroxide precursor [Sn₆O₄(OH)₄] was performed by a precipitation method as described previously [30, 31], with an optimization of several synthesis details in the current study. Starting with 100 ml of a 0.5 M acetic acid aqueous solution, 9.48 grams of SnCl₂·2H₂O (Alfa Aesar 98 %) was completely dissolved at 50°C after constant stirring for 15 minutes. The resulting solution which is cloudy due to SnOCl₂ salt formation [32] was centrifuged to separate a transparent acidic Sn²⁺ solution. Subsequently, a basic solution of ammonium hydroxide (1.13 M) was added dropwise to the acidic Sn²⁺ solution with periodic stirring until the pH level of 4 was reached, leading to the precipitation of a pale-yellow powder. This precipitate was separated by centrifuging and repeated washings with deionized water until of pH value of 7 was reached in order to eliminate residual chlorides followed by drying at 50°C overnight. It is noted that precise synthetic reproducibility of tin(II) oxyhydroxide proved challenging. Further details and opportunities for optimizing the synthesis of this precursor will be discussed in a future publication. In order to make a comparison with the tin(II) oxyhydroxide precursor, a second precursor of conventional tin(II) oxide was prepared from commercial SnO powder (Alfa Aesar 99.9%) after ball milling (FRITSCH planetary micro mill) for two hours in ethanol with 10 mm agate grinding beads in an agate container, followed by drying under air at 80°C for 1 hour).

2.2. SPS Processing

SPS Sintering was performed using Dr. Sinter Lab model SPS-515S with 30kW generator coupled with 50 kN press under dynamic vacuum atmosphere. The precursor powders were loaded into a tungsten carbide (WC) mould assembly (inner ϕ = 10.4 mm with 0.2 mm thick single carbon foils between the powders and inner surface of the mould. Thin carbon and tantalum metal discs were positioned between the precursor powder and WC pistons (top and bottom, along the uniaxial pressure direction) of the mould assembly to reduce reactivity with the sample. Subsequently the WC mould assembly was placed into the SPS chamber and subjected to a computer-controlled cycle of pressure and temperature. For this work, pressure was systematically applied first

(ramp rate of 3.8 kN/min), followed by the desired heating cycle (typically using thermal ramp rates of 25 °C/min, dwell times of 5 mins, and quench cooling). During the entirety of each SPS experiment, the applied piston force and thermocouple temperature of the WC mould assembly was monitored and logged, in addition to other key parameters such as chamber gas pressure, power (voltage, current), and relative piston displacements.

2.3. Material Characterizations

X-ray diffraction (XRD) was performed on precursor powders and ceramics using a Bragg-Brentano geometry PANalytical X'Pert MPD Pro diffractometer with a Cu K α source. Measurements on both powders and ceramics pellets were performed with a 2 θ step size of 0.016° over the 2 θ range 10 – 80°. Analysis of XRD data was performed with the TOPAS software package using a Fundamental Parameters (FP) approach for the instrumental contribution. Starting crystallographic models were obtained from the ICSD database [33] for Sn₆O₄(OH)₄ (N° 203206), SnO (N° 16481) and SnO₂ (N° 183984). Refined terms included: unit cell parameters, background polynomial coefficients, Sn site atomic displacement parameter, and microstructure peak shape profile terms. For some XRD data, in particular for measurements of SPS processed samples, anisotropic strain and March-Dollase type preferred orientation terms were required.

¹¹⁹Sn Mössbauer measurements were performed with a constant acceleration Halder-type spectrometer operating in transmission geometry with a room temperature ^{119m}Sn (CaSnO₃) source (370 MBq). The Mössbauer spectra of thin absorbers containing about 10 mg.cm⁻² of Sn (¹¹⁹Sn natural abundance 8.59%) were recorded at room temperature and the refinement of the Mössbauer hyperfine parameters (δ isomer shift, Δ quadrupole splitting, Γ Lorentzian line width and relative areas) was performed using both homemade programs and the *WinNormos* software (Wissenschaftliche Elektronik GmbH) [34]. The ¹¹⁹Sn isomer shifts are referenced to CaSnO₃ at room temperature.

Sample morphology was examined by SEM (Zeiss EVO 50) in secondary and back-scattering modes. Fourier transform infrared spectroscopy (FTIR, BRUKER Equinox 55) were performed (reflection geometry) to identify functional groups in starting precursor powders. Thermogravimetric analysis (TGA, TA-Q50) of precursor powders were performed under flowing air with 5°C/min temperature ramps. Electrical resistivity measurements were performed with a homemade four-point probe setup, using tungsten carbide needles (ϕ = 100 μ m) with 1 mm spacing. A DC current source (0.1 mA) used by the instrument ADRET 103A while the temperature was regulated by a Eurotherm 902 (PT100 sensor). Electrochemical Impedance Spectroscopy (EIS) measurements were performed at room temperature with Autolab potentiostat/galvanostat (PSTAT302N) with FRA32M module for a frequency range of 10Hz-1MHz.

3. Results and Discussion

3.1. Concerning the Precursor Powders

The tin(II) oxyhydroxide precursor was synthesised as described in section 2.1, with an end product appeared to be pale yellow in color after final drying. Initial characterization of the powder by XRD and FTIR suggested a largely phase pure material consistent with previous reports on the composition Sn₆O₄(OH)₄ [35, 36]. The main plot in Fig. 1a shows the single-phase Rietveld fit, using the tetragonal *P*-42₁/*c* space group with refined values for lattice [a = 7.952(1) Å, c = 9.139(1) Å] and crystallite size (giving a volume weighted integral breadth estimate of < 200 nm). The inset of Fig. 1a shows the FTIR spectrum, with strong but broad absorption peaks around 3400 cm⁻¹ and 550 cm⁻¹, which can be associated with hydroxide O-H group stretching and Sn-O bond stretching, respectively. SEM imaging (Fig. 2a) displays a homogenous distribution of fine sub-micron sized agglomerated particles.

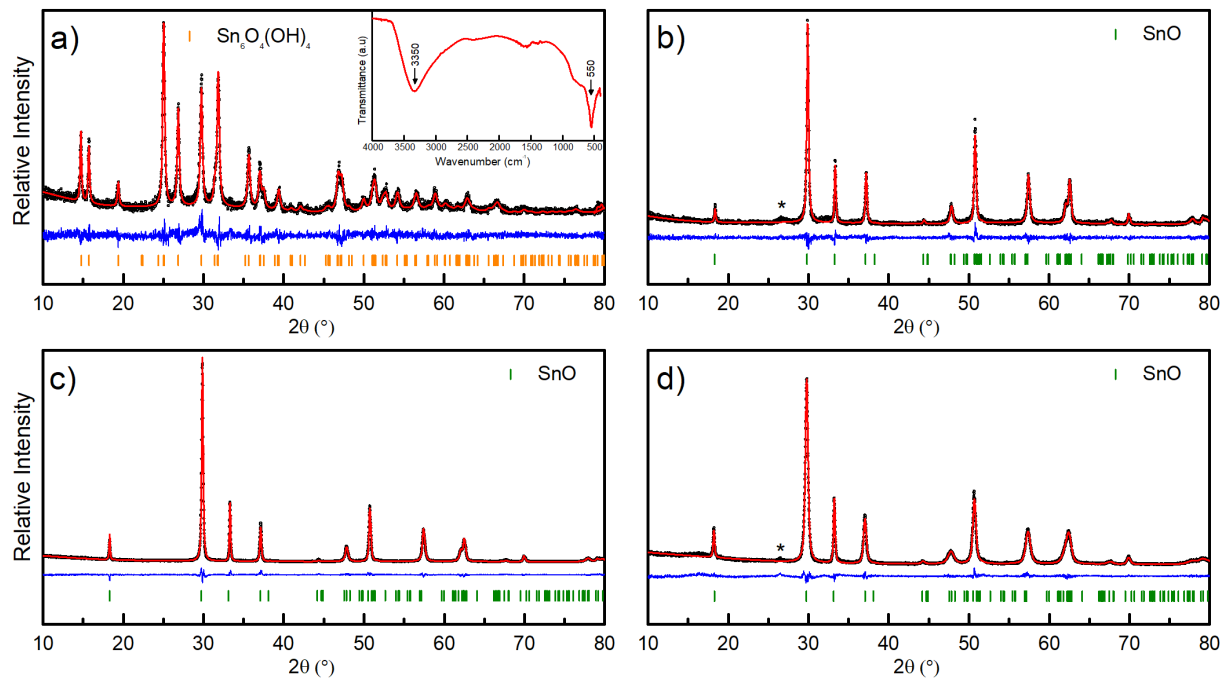


Fig. 1. Rietveld refinement fit profiles of powder XRD data measured on (a) starting tin(II) oxyhydroxide precursor powders and (b) the resulting SPS ceramic, followed by (c) the initial ball-milled SnO precursor and (d) corresponding ceramic after SPS processing. Each main plot displays Y_{obs} (black points), Y_{calc} (red line), a fit difference curve (blue line), and vertical phase tickmarks. Asterisks mark the position of minor SnO₂ phase peaks. The inset of Fig. 1(a) displays the FTIR spectra for tin(II) oxyhydroxide precursor.

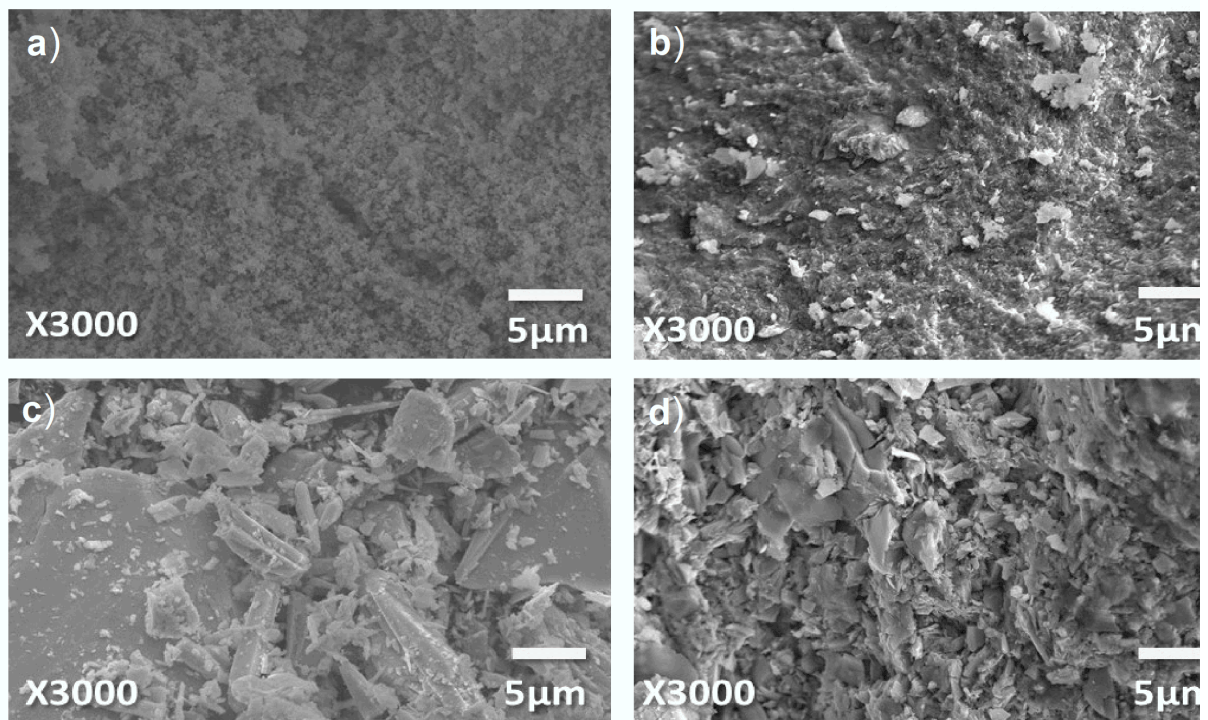


Fig. 2. SEM micrographs at top of initial (a) tin(II) oxyhydroxide precursor powders and (b) fractured surface of the resulting ceramic. In parallel, at bottom, micrographs of (c) conventional ball-milled SnO powders and (d) a fractured surface of the ceramic after processing.

TGA analysis of the tin(II) oxyhydroxide precursor under air shows a curve (Fig. 3, red line) which is also in good agreement with previous reports [37]. An initial weight loss of $\sim 2.5\%$ below $200\text{ }^{\circ}\text{C}$ is observed and is attributed to the release of hydroxide groups to form SnO (vs. an expected theoretical weight loss for $\text{Sn}_6\text{O}_4(\text{OH})_4 \rightarrow \text{SnO}$ of 4.3%). Above $200\text{ }^{\circ}\text{C}$, further heating under air results in weight gain associated with the oxidation of SnO $\rightarrow \text{SnO}_2$. The weight gain increases sharply with temperature, before abruptly flattening above $380\text{ }^{\circ}\text{C}$, at which point the oxidation of Sn^{2+} to Sn^{4+} may be largely complete. However, the observed experimental gain between $200\text{ }^{\circ}\text{C}$ and $400\text{ }^{\circ}\text{C}$ of $\sim 5\%$ is less than the expected theoretical weight gain of 11.9% for $\text{SnO} \rightarrow \text{SnO}_2$.

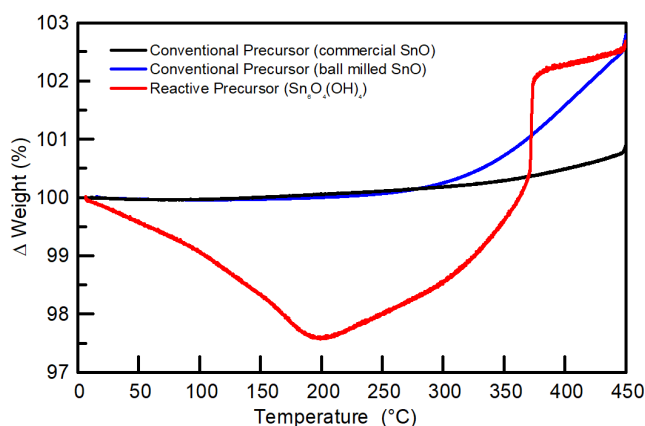


Fig. 3. Comparison of TGA measurements performed on heating under air ($5\text{ }^{\circ}\text{C}/\text{min}$) for different precursor powders.

Further analysis of the fragile tin(II) oxyhydroxide precursor powder by ^{119}Sn Mössbauer helps understand these discrepancies in observed TGA weight gain/loss. A typical fit of the experimentally measured spectra (Fig. 4a) shows the expected doublet with isomer shift characteristic of divalent Sn^{2+} (blue shaded area), but also the significant signature of a singlet doublet with near-zero isomer shift characteristic of Sn^{4+} (green shaded area). Semi-quantitative analysis estimates the Sn^{4+} fraction at approximately 40% . Subsequent re-analysis by powder XRD with an internal standard for quantification of non-crystalline content, indicates that amorphous phase(s) make up approximately 30% mass fraction of the sample, which is assumed to incorporate the Sn^{4+} species observed by Mössbauer analysis. This apparent reduction in divalent tin containing phases participating in decomposition/oxidation processes is qualitatively consistent with the smaller than theoretically expected mass changes measured in TGA.

Despite repeated attempts to optimize the synthesis conditions for tin(II) oxyhydroxide, it was not possible to fully eliminate this amorphous content. It is speculated that some level of undetected amorphous Sn^{4+} material was also present in $\text{Sn}_6\text{O}_4(\text{OH})_4$ powders examined by multiple previous literature reports [11, 31]. Enhancement of synthesis parameters will be investigated further in future publications. Nevertheless, as discussed below, the tin(II) oxyhydroxide powder obtained in the current study was sufficient to demonstrate the unique possibility of fragile precursors as a processing route for Sn^{2+} containing ceramic oxides by Cool-SPS.

The reactive nature of the powders encompasses both a small particle size distribution and its propensity for reactivity at low temperatures. For the later aspect, TGA analysis was used to assess and compare with conventional tin(II) oxide precursor powders. As shown in Fig. 3 (black line), the as-received commercial SnO powder remains relatively inert under air up to $350\text{ }^{\circ}\text{C}$, with $< 1\%$ weight gain from oxidation even at $400\text{ }^{\circ}\text{C}$. However, the decreased agglomerate sizes resulting from only 2 hours of ball milling lowers the onset temperature of decomposition/oxidation processes, with a clear mass increase starting from $300\text{ }^{\circ}\text{C}$ (blue line,

Fig. 3). SEM images after ball milling (Fig. 2c) show an inhomogeneous distribution of particle sizes. These results agree well with the previous report of Bang *et al.*, in which a further reduction in decomposition temperature is observed after 24 hours of SnO ball milling [26]. However the tin(II) oxyhydroxide of the current study extends this trend even farther, with a lower onset temperature and larger relative weight gains after the release of hydroxide groups from 200 °C. Note that phase purity of the precursor SnO powder appears unaffected by ball milling, as assessed by both a single-phase Rietveld fit of XRD data [Fig. 1c, tetragonal space group $P4/nmm$ with refined lattice parameters of $a = 3.802(1)$ Å, $c = 4.841(1)$ Å, in excellent accord with ICSD database values] and clean divalent Sn doublet observed by Mössbauer analysis (Fig. 4c).

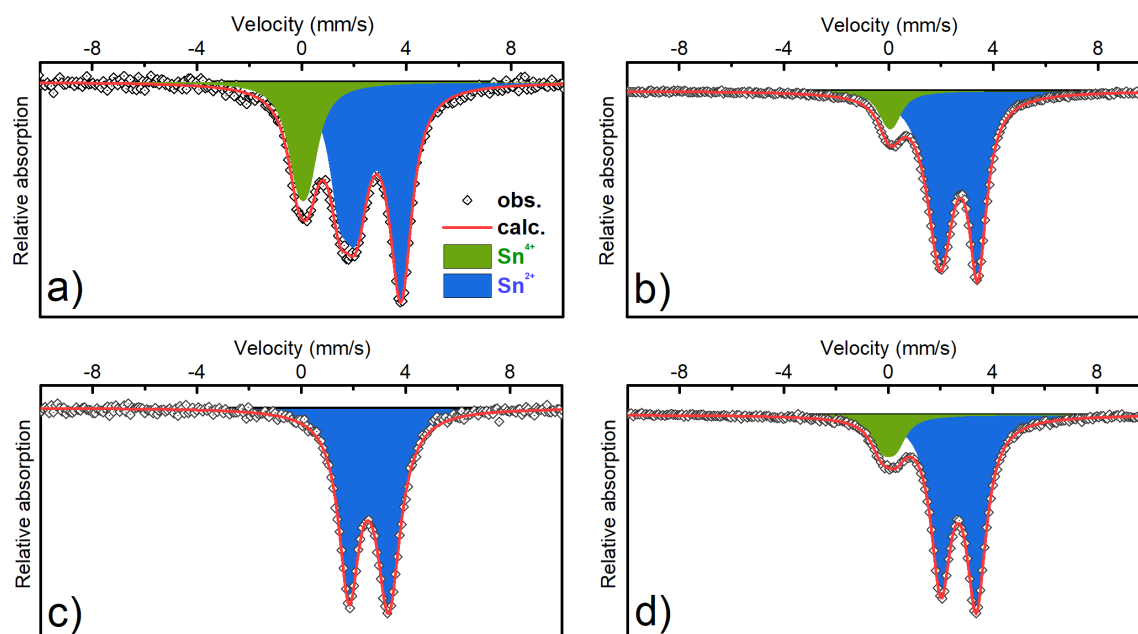


Fig. 4. Room temperature ^{119}Sn Mössbauer spectra for the (a) tin(II) oxyhydroxide precursor and (b) resulting sample after SPS processing; similarly (c) for the conventional ball-milled SnO powder and (d) corresponding sample after SPS processing. Green and blue shaded areas of the spectra indicate the fitted fractions for Sn^{2+} and Sn^{4+} environments, respectively.

3.2. Processing Parameters

Using low temperature Cool-SPS processing conditions to target dense SnO ceramics, a study was made comparing the impact and efficiency of the different precursor powders. For both the fragile tin(II) oxyhydroxide and conventional SnO powders, a wide range of different pressure and temperature parameters were explored in order to establish optimized processing conditions for each. As discussed earlier in section 2.2., pressure was systematically applied first during SPS processing, followed by a programmed thermal ramp at constant pressure which lead to dwell period (typically ~ 5 minutes) at constant pressure and temperature. The processing cycle was completed by a rapid cooling in < 5 minutes to ambient temperature, and subsequent decompression, in order to extract the sample from the SPS mould assembly for characterization.

Real-time monitoring of several SPS parameters during processing provides indirect insight into the sequence of reaction mechanisms occurring under different conditions. This is illustrated in Fig. 5a and Fig. 5b, which plots the evolution of two parameters; Piston Displacement and Chamber Pressure, left and right axes respectively, during processing. Piston Displacement (units of mm) provides information about sample compaction or densification; although impossible to separate from the contributions of the mould and spacers - larger values of displacement can be associated with decreasing sample thickness (as the upper plate in the SPS chamber is fixed). Chamber Pressure (units of Pa) is qualitatively connected to sample outgassing events, such

as the release of hydroxide groups. Higher chamber pressure values indicate larger outgassing volumes, but without any specific information on the chemical nature of these species.

This is illustrated in Fig. 5a, where these parameters are plotted for a typical SPS processing sequence of conventional ball-milled SnO precursor powders. Starting from the left side of the plot, the initial ambient temperature sample compaction with increasing load is observed. Next, the sample temperature is increased while maintaining the constant target force (400 MPa in this example). With temperature increase, a small raise in chamber pressure (likely chemisorbed water) is noted after 100 °C, but little further sample densification is observed suggesting densification is mainly dependent on pressure-driven mechanisms. In the third sequence step, a 5-minute dwell at constant temperature and compression (300 °C and 400 MPa), the minor outgassing events subside. Outgassing continues to decrease during the last quench cooling and de-compression steps, with an initial contraction of the sample dimensions upon cooling before a final expansion as the piston pressure is released.

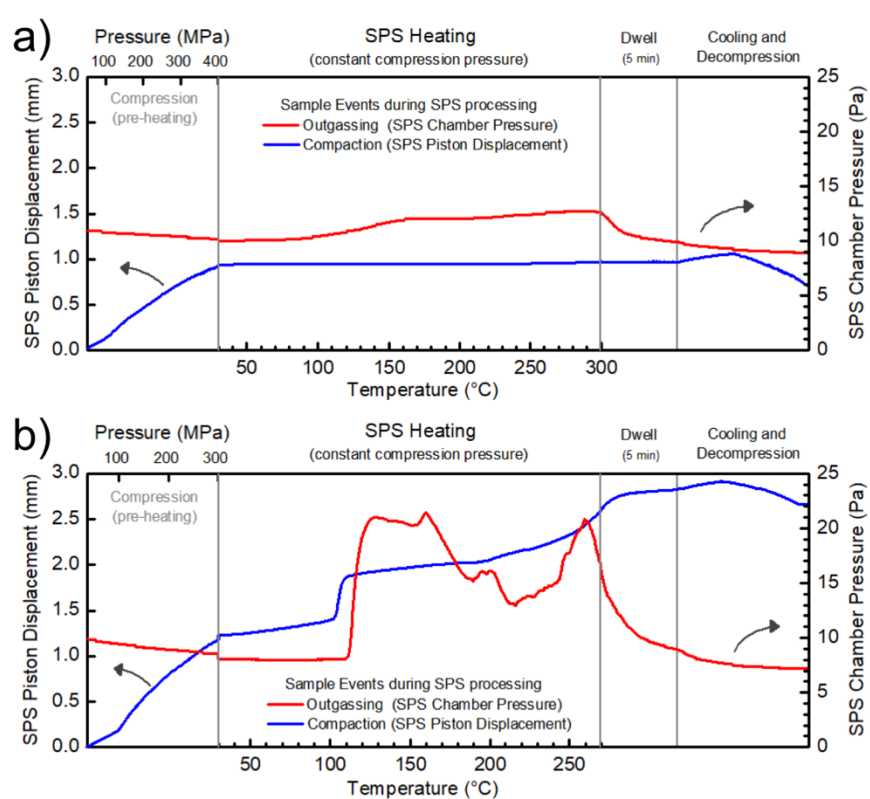


Fig. 5. Schematic plots showing the typical evolution of two SPS monitoring parameters discussed in the main text over the entire processing sequence for (a) conventional SnO and (b) fragile tin(II) oxyhydroxide precursor powders. Sample compaction is directly related to Piston Displacement (red lines, left axis), while decomposition and sample outgassing events are inferred from Chamber pressure values (blue lines, right axis).

By contrast, monitored parameters from processing of fragile tin(II) oxyhydroxide precursors (Fig. 5b) reveal different mechanisms in play especially during heating. While the initial sample compaction at ambient temperature is similar to conventional SnO (up to 300 MPa), significant outgassing and densification events are observed during the heating step. Starting from 100 °C, an abrupt sample compaction is presumably connected to the almost simultaneous onset of a significant outgassing event that continues beyond ~ 160 °C. It is assumed this is associated with the initial decomposition of tin(II) oxyhydroxide and the release of OH groups. A later increase in outgassing just prior to the constant temperature plateau of 270 °C is also associated with increased sample compaction. Subsequently, on cooling and de-compression, the trends echo that seen in Fig. 5a, hinting

at the fact that the final processed samples from both processing routes are similar. However, it is clear that the chemical reaction paths and compaction mechanisms followed to arrive at a dense SnO ceramic varies significantly during low temperature SPS processing depending on the choice of initial starting precursor powders.

It is noted that direct comparisons with complementary TGA data under air on the same precursor powders is complicated by unique heating mechanism and sample environment of the SPS mould and the dynamic vacuum atmosphere of the SPS chamber. Moreover, the combination of carbon foils and a dynamic vacuum creates reducing conditions in the SPS chamber. Thus, some speculation on chemical reaction routes is unavoidable in the absence of direct chemical information on the outgassing species; future SPS experiments incorporating residual gas analysis are planned.

3.3. Sintering and Phase Stability

Numerous experiments on both conventional and fragile precursor powders were examined in the current study in order to understand and optimize the processing sequences for each precursor. In particular, these results have been compared with recent work on SnO densification by a CSP approach [26]. Table 1 lists the experimental SPS temperature and pressure conditions, and resulting geometric pellet density for selected attempts. The attempts performed at 265 °C and 350 MPa (using commercial and ball-milled SnO precursor powders, respectively) were selected for direct comparison with the optimized CSP parameters recently reported by Bang *et al.* For both CSP and SPS, ball milling of the commercial SnO precursor consistently appears to promote greater densification. However, initial targeting of the same plateau parameters (265 °C and 350 MPa) in the current SPS study resulting in pellet densities (72 and 78%, for commercial and ball-milled powders, respectively) notably lower than that achieved with CSP (84 and 89%, respectively) under the same nominal temperature and physical pressure conditions [26]. Two important experimental differences may help explain these results. Firstly; in the CSP approach, the total processing time (ramp and dwell) is much longer; more than 100 minutes for the reported CSP work on SnO compared with under 30 minutes for SPS in the current study. Secondly, and perhaps more importantly, the CSP study of Bang *et al.* made use of additional transient liquids to promote dissolution/precipitation processes.

Table 1

Summary of final geometric ceramic densities (% of theoretical density) and corresponding precursor and SPS processing conditions for selected SnO samples discuss in the main text.

Precursor Powder	Temp. (°C)	Pressure (MPa)	Dwell Time	Ceramic Density
SnO (commercial)	265	350	5 min	72 %
SnO (Ball Milled)	265	350	5 min	78 %
SnO (Ball Milled)	300	400	5 min	91 %
Tin(II) Oxyhydroxide	270	300	5 min	90 %

Additional experiments to explore SPS processing parameters for ball milled commercial SnO powders have demonstrated that improved ceramic densities of approximately 90% can be achieved at slightly higher temperature and pressure values (Table 1, line 3). Optimal conditions were found when using at least 400 MPa of compression pressure at a dwell temperature of approximately 300 °C. Refinement of XRD data (Fig. 1d) from the resulting pellet shows a new single phase SnO sample (*P4/nmm* with $a = 3.801(1) \text{ \AA}$, $c = 4.839(1) \text{ \AA}$). A weak peak in the background attributed to a minor SnO₂ contamination is marked by asterisk. This is in good agreement with Mössbauer analysis (Fig. 4d) showing the expected dominant doublet peak for divalent Sn²⁺ (blue shaded area, ~ 90%) with a minor divalent Sn²⁺ (blue shaded area, ~ 10%). In general, lower values of

pressure and temperature produced pellets with inferior geometric density values. Greater pressure values (> 400 MPa) did not improve final pellet densities, and instead decreased the likelihood of successfully extracting intact samples from the WC mould. The upper temperature limit for SnO phase stability under SPS processing parameters explored in this study varied inversely with pressure, decreasing from approximately 500 °C at 50 MPa to approximately 300 °C at 600 MPa. Experiments performed with processing parameters beyond these thermodynamic limits consistently exhibited evidence of significant decomposition / disproportion of SnO towards SnO₂ and metallic Sn.

A similar exploration of processing parameters was undertaken for the fragile tin(II) oxyhydroxide precursor. Consistent with the TGA results (Fig. 3), these precursor powders showed greater thermal reactivity, in particular at lower compression pressures. The upper temperature limit for phase stability was also reduced; evidence for significant SnO₂ and/or metallic Sn formation started from 350 °C even at lower pressures of 50 MPa. But most significantly, it was demonstrated that tin(II) oxyhydroxides precursors can be used to realize robust SnO ceramics with geometric densities and phase purities equivalent to that obtained with conventional SnO precursors. Optimal processing conditions are found when using 300 MPa compression pressure and a dwell temperature of approximately 270 °C (Table 1, line 4). Resulting XRD data and Mössbauer data are very similar to those observed for samples derived from conventional SnO precursors. XRD refinements (Fig. 1b) show a SnO phase (*P4/nmm* with $a = 3.803(1)$ Å, $c = 4.836(1)$ Å), again with minor SnO₂ contamination. Mössbauer analysis (Fig. 4b) reveal almost identical spectra (with ~ 90/10% fractions for Sn²⁺ and Sn⁴⁺, respectively). Critically, it is noted that within the optimized processing limits for the tin(II) oxyhydroxide precursor, the reducing environment promotes conversion of Sn⁴⁺ to divalent Sn; while limited tetravalent tin is formed during processing of the conventional SnO precursor. This is revealed by the Mössbauer analysis, where the fraction of Sn⁴⁺ is diminished following processing (Figs. 4a, 4b), while Sn⁴⁺, absent from the initial SnO conventional precursor, is observed in the ceramics (Figs 4c, 4d). With the tin(II) oxyhydroxide precursor, no evidence of improved densities was found for greater compression pressures up to 500 MPa. Dwell temperatures down to even 200 °C resulted in ceramic densities of at least 85%. Cohesive samples were difficult to obtain outside the window of these optimized processing parameters. Ensuring that the largest outgassing event preceded the dwell plateau temperature during the processing sequence (Fig. 5b) was critical in achieving the best SnO phase purity of the resulting ceramic.

Taken together, these results clearly demonstrate that densification of Sn(II)-based oxides by SPS can offer certain advantages in overall processing time and phase stability when compared to other approaches. Moreover, through a Cool-SPS type processing strategy and the use of tin(II) oxyhydroxide precursors, it is possible to achieve ceramics with equivalent phase purity and geometric density at reduced temperature and applied pressure processing conditions. With further optimization of tin(II) oxyhydroxide precursors, it is expected that SnO ceramics with pure divalent tin content can be achieved in view of the active reducing tendencies of the optimized processing conditions. Our results also reveal that the choice of precursor strongly influences the resulting microstructure of the dense SnO ceramics. The comparison of SEM micrographs from ball-milled SnO precursor powders (Fig. 2c) with the resulting dense pellet (Fig. 2d) shows the expected increase in densification but reveals that the initial inhomogeneous distribution of particle sizes is partially maintained after processing. However, SEM examination of the ceramic fracture surface obtained from the tin(II) oxyhydroxide precursor (Fig. 2b) displays a very different dense, homogeneous and fine grained microstructure. Despite limited SEM spatial resolution and the use of anisotropic peak shape profiles in XRD data refinements which prevent an accurate determination of crystallite domain sizes, these contrasting differences in grain size and densification morphology are shown below to strongly impact physical properties of the resulting SnO ceramics.

3.5 Transport Characterizations

Bulk transport properties of dense SnO ceramics were characterized by variable temperature DC conductivity and room temperature AC impedance spectroscopy measurements. These results are shown in Fig. 6. Significant differences in the conductivity values and temperature behavior of DC conductivity are found between densified ceramics obtained from conventional SnO precursors and those derived from fragile tin(II) oxyhydroxide precursors (Fig. 5a). For the sample originating from conventional SnO powders, a modest increase in conductivity with temperature over the range 25 – 220 °C is observed, as expected for a *p*-type semiconductor [7]. The measured room temperature DC conductivity of 0.06 S/cm is slightly higher but not inconsistent with a predicted value of ~ 0.03 S/cm [15]. Similar but somewhat lower experimental values of ~ 0.01 S/cm are recently reported for SnO pellets with equivalent densities processed by CSP [26]; minor differences in sample processing or measurement details might explain this range of DC conductivity values. In contrast, tin(II) oxyhydroxide precursors produced ceramics with DC conductivities near 1×10^{-3} S/cm; roughly two orders of magnitude lower than that measured on ceramics derived from the conventional SnO precursor. Moreover, a non-linear thermal dependence of conductivity is observed. It is proposed that these contrasting properties are linked with the dissimilarities in final pellet microstructures between the two processing routes. For the fragile oxyhydroxide route samples, overall sample conductivity is likely reduced by more substantial grain boundary effects accompanying the fine grain sizes (see SEM micrographs, Fig. 2b), or by disordered interface layers between grains. The thermal dependence may be correlated with greater interfacial contributions that vary with temperature under non-reducing atmospheres.

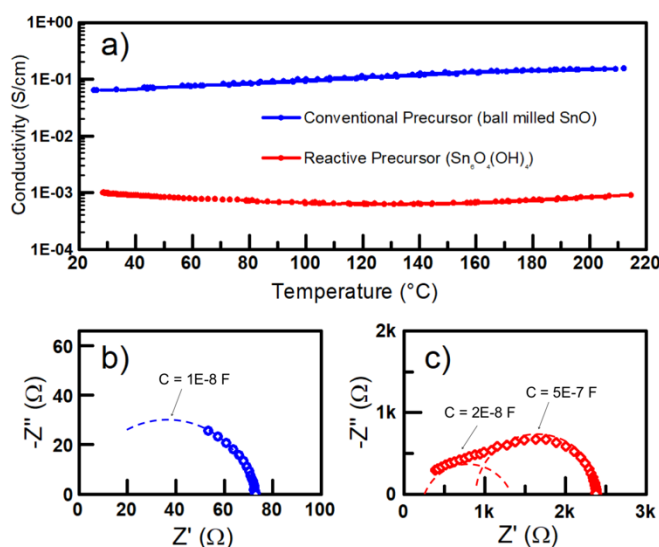


Fig. 6. Variable temperature DC conductivity measurements of SnO pellets (a) obtained after processing from conventional and fragile precursor powders (blue and red points, respectively). Ambient temperature Cole-Cole type plots for frequency dependent EIS analysis of samples obtained from (b) conventional SnO and (c) fragile tin(II) oxyhydroxide precursor powders.

A preliminary evaluation of electrochemical conduction mechanisms was performed with ambient temperature AC electrochemical impedance spectroscopy (EIS). Plotted as Nyquist type plots, the EIS results are consistent with the DC conductivity data, in that the conventional SnO precursors pellets (Fig. 5b) exhibit much lower bulk sample impedance values than what is measured on ceramics derived from fragile oxyhydroxide precursors (Fig. 5c). In the low frequency DC limit, the extrapolated *x*-axis intercept *Z'* values are 75 Ω and 2400 Ω, respectively. Within the limits of the used frequency ranges, an analysis attempt to extract capacitance values for different features of the Nyquist plots was performed with the equation $\omega_{\max}RC = 1$ [38]. For conventional

SnO precursor derived ceramics (Fig. 5b), this gives a single feature with $C = 1 \times 10^{-8}$ F; while for ceramics derived from tin (II) oxyhydroxide precursors (Fig. 5c) two features with $C = 2 \times 10^{-8}$ F and with $C = 5 \times 10^{-7}$ F are estimated. The smaller near-equivalent capacitive features may represent the similar bulk phenomenon, with the second larger capacitive feature in the latter providing further evidence of additional grain boundary effects in sintered SnO ceramics derived from the oxyhydroxide precursors. Further investigation, in particular variable temperature EIS beyond the scope of this study, is needed to fully elucidate the electrochemical and microstructural characteristics of SPS sintered SnO ceramics.

4. Conclusions

In the pursuit of achieving dense SnO ceramics, an efficient approach has been successfully demonstrated, affording rapid densification to 90% of theoretical density. This approach offers flexibility in the choice of starting precursor chemistry, working well with both conventional ball-milled SnO and fragile tin(II) oxyhydroxide precursor powders, although care must be taken to track and optimize processing parameters in each case. Extensive characterization of samples before and after processing by XRD, FTIR, TGA, and ^{119}Sn -Mossbauer spectroscopy provides details concerning phase content and Sn oxidation state. Interestingly, under appropriate temperature and pressure conditions, the Cool-SPS route actively promotes stability of the desired Sn^{2+} species. It is also found that the nature of the starting precursor strongly impacts the final sintered SnO microstructure, which subsequently affects the bulk electrochemical properties. With a strategic selection of precursors, it is possible to achieve significant reductions in overall sample conductivity, which can present opportunities for exploiting the possible ferroelectric response of lone-pair Sn^{2+} cations. Although only the simple case of SnO is explored in the current work, the rapid processing times, chemical flexibility and resulting tuning of structure/property relationships offered by a low temperature Cool-SPS approach likely offers interesting avenues of future exploration for more complex Sn(II) based oxide systems.

Declaration of Competing Interest

The authors report no declaration of interest.

Acknowledgements

We thank the Université de Bordeaux and MESRI for PhD fellowship funding (SBB) and a 6 months sabbatical to develop Cool-SPS, following the “délégation” previously awarded by CNRS (MJ). We greatly appreciate the technical assistance and discussions concerning sample characterization provided by colleagues at both the ICMCB (Laetitia ETIENNE, Fabrice MAUVY, Rodolphe DECOURT, and Stéphane RELEXANS) and PLACAMAT (UMS 3626, Philippe LEGROS).

References

- [1] Preparation of protoxide of tin, *The London, Edinburgh, and Dublin Philosophical Magazine and Journal of Science*. 31 (1847) 392–392. <https://doi.org/10.1080/14786444708645876>.
- [2] A. Ditte, Action des dissolutions acides sur le protoxyde d'étain, *Compt. Rend.* 94 (1882) 792.
- [3] W. Kwestroo, P.H.G.M. Vromans, Preparation of three modifications of pure tin (II) oxide, *J. Inorg. Nuc. Chem.* 29 (1967) 2187–2190. [https://doi.org/10.1016/0022-1902\(67\)80273-2](https://doi.org/10.1016/0022-1902(67)80273-2).
- [4] W.J. Moore Jr, L. Pauling, The Crystal Structures of the Tetragonal Monoxides of Lead, Tin, Palladium, and Platinum, *J. Am. Chem. Soc.* 63 (1941) 1392–1394. <https://doi.org/10.1021/ja01850a074>.
- [5] J. Pannetier, G. Denes, Tin(II) oxide: structure refinement and thermal expansion, *Acta Crystallogr B Struct Sci.* 36 (1980) 2763–2765. <https://doi.org/10.1107/S0567740880009934>.
- [6] S.E. Dunkle, J.R. Craig, J.D. Rimstidt, W.R. Lusardi, Romarchite, Hydromorarchite And Abhurite Formed During The Corrosion Of Pewter Artifacts From The Queen Anne's Revenge (1718), *Canad Mineral.* 41 (2003) 659–669. <https://doi.org/10.2113/gscanmin.41.3.659>.
- [7] Y. Ogo, H. Hiramatsu, K. Nomura, H. Yanagi, T. Kamiya, M. Kimura, M. Hirano, H. Hosono, Tin monoxide as an s-orbital-based p-type oxide semiconductor: Electronic structures and TFT application, *Phys. Stat. Sol. (a)*. 206 (2009) 2187–2191. <https://doi.org/10.1002/pssa.200881792>.
- [8] P.H. Suman, A.A. Felix, H.L. Tuller, J.A. Varela, M.O. Orlandi, Comparative gas sensor response of SnO₂, SnO and Sn₃O₄ nanobelts to NO₂ and potential interferents, *Sensors and Actuators B: Chemical*. 208 (2015) 122–127. <https://doi.org/10.1016/j.snb.2014.10.119>.
- [9] K.J. Saji, Y.P. Venkata Subbaiah, K. Tian, A. Tiwari, P-type SnO thin films and SnO/ZnO heterostructures for all-oxide electronic and optoelectronic device applications, *Thin Solid Films*. 605 (2016) 193–201. <https://doi.org/10.1016/j.tsf.2015.09.026>.
- [10] K. Okamura, B. Nasr, R.A. Brand, H. Hahn, Solution-processed oxide semiconductor SnO in p-channel thin-film transistors, *J. Mater. Chem.* 22 (2012) 4607. <https://doi.org/10.1039/c2jm16426d>.
- [11] J. Ning, T. Jiang, K. Men, Q. Dai, D. Li, Y. Wei, B. Liu, G. Chen, B. Zou, G. Zou, Syntheses, Characterizations, and Applications in Lithium Ion Batteries of Hierarchical SnO Nanocrystals, *J. Phys. Chem. C*. 113 (2009) 14140–14144. <https://doi.org/10.1021/jp905668p>.
- [12] S. Jaśkaniec, S.R. Kavanagh, J. Coelho, S. Ryan, C. Hobbs, A. Walsh, D.O. Scanlon, V. Nicolosi, Solvent engineered synthesis of layered SnO for high-performance anodes, *Npj 2D Mater Appl.* 5 (2021) 27. <https://doi.org/10.1038/s41699-021-00208-1>.
- [13] L. Seixas, A.S. Rodin, A. Carvalho, A.H. Castro Neto, Multiferroic Two-Dimensional Materials, *Phys. Rev. Lett.* 116 (2016) 206803. <https://doi.org/10.1103/PhysRevLett.116.206803>.
- [14] M. Houssa, K. Iordanidou, G. Pourtois, V.V. Afanas'ev, A. Stesmans, Ferromagnetism in two-dimensional hole-doped SnO, *AIP Advances*. 8 (2018) 055010. <https://doi.org/10.1063/1.5025272>.
- [15] S.A. Miller, P. Gorai, U. Aydemir, T.O. Mason, V. Stevanović, E.S. Toberer, G.J. Snyder, SnO as a potential oxide thermoelectric candidate, *J. Mater. Chem. C*. 5 (2017) 8854–8861. <https://doi.org/10.1039/C7TC01623A>.
- [16] M. Moreno, Kinetic study of the disproportionation of tin monoxide, *Solid State Ionics*. 144 (2001) 81–86. [https://doi.org/10.1016/S0167-2738\(01\)00882-7](https://doi.org/10.1016/S0167-2738(01)00882-7).
- [17] H. Giefers, F. Porsch, G. Wortmann, Kinetics of the disproportionation of SnO, *Solid State Ionics*. 176 (2005) 199–207. <https://doi.org/10.1016/j.ssi.2004.06.006>.
- [18] C.M. Campo, J.E. Rodríguez, A.E. Ramirez, Thermal behaviour of romarchite phase SnO in different atmospheres: a hypothesis about the phase transformation, *Heliyon*. 2 (2016) e00112. <https://doi.org/10.1016/j.heliyon.2016.e00112>.
- [19] M. Biesuz, S. Grasso, V.M. Sglavo, What's new in ceramics sintering? A short report on the latest trends and future prospects, *Current Opinion in Solid State and Materials Science*. 24 (2020) 100868. <https://doi.org/10.1016/j.cossms.2020.100868>.
- [20] H. Kähäri, M. Teirikangas, J. Juuti, H. Jantunen, Dielectric Properties of Lithium Molybdate Ceramic Fabricated at Room Temperature, *J. Am. Ceram. Soc.* 97 (2014) 3378–3379. <https://doi.org/10.1111/jace.13277>.
- [21] J. Guo, H. Guo, A.L. Baker, M.T. Lanagan, E.R. Kupp, G.L. Messing, C.A. Randall, Cold Sintering: A Paradigm Shift for Processing and Integration of Ceramics, *Angew. Chem.* 128 (2016) 11629–11633. <https://doi.org/10.1002/ange.201605443>.
- [22] A. Ndayishimiye, M.Y. Sengul, T. Sada, S. Dursun, S.H. Bang, Z.A. Grady, K. Tsuji, S. Funahashi, A.C.T. van Duin, C.A. Randall, Roadmap for densification in cold sintering: Chemical pathways, *Open Ceramics*. 2 (2020) 100019. <https://doi.org/10.1016/j.oceram.2020.100019>.

- [23] T. Herisson de Beauvoir, A. Sangregorio, I. Cornu, C. Elissalde, M. Josse, Cool-SPS: an opportunity for low temperature sintering of thermodynamically fragile materials, *J. Mater. Chem. C*. 6 (2018) 2229–2233. <https://doi.org/10.1039/C7TC05640K>.
- [24] D. Sohrabi Baba Heidary, M. Lanagan, C.A. Randall, Contrasting energy efficiency in various ceramic sintering processes, *Journal of the European Ceramic Society*. 38 (2018) 1018–1029. <https://doi.org/10.1016/j.jeurceramsoc.2017.10.015>.
- [25] C. Elissalde, U.-C. Chung, M. Josse, G. Goglio, M.R. Suchomel, J. Majimel, A. Weibel, F. Soubie, A. Flaureau, A. Fregeac, C. Estournès, Single-step sintering of zirconia ceramics using hydroxide precursors and Spark Plasma Sintering below 400 °C, *Scripta Materialia*. 168 (2019) 134–138. <https://doi.org/10.1016/j.scriptamat.2019.04.037>.
- [26] S.H. Bang, T. Herisson De Beauvoir, C.A. Randall, Densification of thermodynamically unstable tin monoxide using cold sintering process, *J. Eur. Ceram. Soc.* 39 (2019) 1230–1236. <https://doi.org/10.1016/j.jeurceramsoc.2018.11.026>.
- [27] G. Franceschin, N. Flores-Martínez, G.V. Victorio, S. Ammar, R. Valenzuela, Sintering and Reactive Sintering by Spark Plasma Sintering (SPS), in: I. Shishkovsky (Ed.), *Sintering of Functional Materials*, InTech, 2018. <https://doi.org/10.5772/intechopen.68871>.
- [28] T. Herisson de Beauvoir, V. Villemot, M. Josse, Cool-Spark plasma sintering: An opportunity for the development of molecular ceramics, *Solid State Sciences*. 102 (2020) 106171. <https://doi.org/10.1016/j.solidstatesciences.2020.106171>.
- [29] T. Hérisson de Beauvoir, F. Molinari, U.C. Chung-Seu, D. Michau, D. Denux, M. Josse, Densification of MnSO₄ ceramics by Cool-SPS: Evidences for a complex sintering mechanism and magnetoelectric coupling, *Journal of the European Ceramic Society*. 38 (2018) 3867–3874. <https://doi.org/10.1016/j.jeurceramsoc.2018.04.005>.
- [30] J.D. Donaldson, W. Moser, Hydrous Tin(II) Oxide, *J. Chem. Soc.* (1961) 835–838. <https://doi.org/10.1039/JR9610000835>.
- [31] S. Kitabayashi, N. Koga, Thermal Decomposition of Tin(II) Oxyhydroxide and Subsequent Oxidation in Air: Kinetic Deconvolution of Overlapping Heterogeneous Processes, *J. Phys. Chem. C*. 119 (2015) 16188–16199. <https://doi.org/10.1021/acs.jpcc.5b04975>.
- [32] Wiberg, E., Wiberg, N., Holleman, A.F., 2001. *Inorganic chemistry*. Academic Press ; De Gruyter, 1st ed. San Diego, Calif., 2001.
- [33] D. Zagorac, H. Müller, S. Ruehl, J. Zagorac, S. Rehme, Recent developments in the Inorganic Crystal Structure Database: theoretical crystal structure data and related features, *J Appl Crystallogr.* 52 (2019) 918–925. <https://doi.org/10.1107/S160057671900997X>.
- [34] Brand, R. A. WinNormos Mössbauer Fitting Program; Universität Duisburg, 2008.
- [35] I. Abrahams, S.M. Grimes, S.R. Johnston, J.C. Knowles, Tin(II) Oxyhydroxide by X-ray Powder Diffraction, *Acta Crystallogr. C*. 52 (1996) 286–288. <https://doi.org/10.1107/S0108270195012625>.
- [36] H. Deng, J.M. Hossenlopp, Combined X-ray Diffraction and Diffuse Reflectance Analysis of Nanocrystalline Mixed Sn(II) and Sn(IV) Oxide Powders, *J. Phys. Chem. B*. 109 (2005) 66–73. <https://doi.org/10.1021/jp047812s>.
- [37] J. Khanderi, L. Shi, A. Rothenberger, Hydrolysis of bis(dimethylamido)tin to tin (II) oxyhydroxide and its selective transformation into tin (II) or tin (IV) oxide, *Inorganica Chimica Acta*. 427 (2015) 27–32. <https://doi.org/10.1016/j.ica.2014.11.031>.
- [38] J.T.S. Irvine, D.C. Sinclair, A.R. West, Electroceramics: Characterization by Impedance Spectroscopy, *Adv. Mater.* 2 (1990) 132–138. <https://doi.org/10.1002/adma.19900020304>.